Design of a PET/MRI DOI Detector Consisting of a Quasi-Block Scintillator and a Dual-Sided Readout Photosensor with MLPE in a High Magnetic Field

Seung-Jae Lee^{1,2} and Cheol-Ha Baek^{3*}

¹Department of Radiological Science, Dongseo University, Busan 47011, Republic of Korea ²Center for Radiological Environment & Health Science, Dongseo University, Busan 47011, Republic of Korea ³Department of Radiological Science, Kangwon National University, Gangwon 25949, Republic of Korea

(Received 12 July 2025, Received in final form 2 September 2025, Accepted 3 September 2025)

The spatial resolution of small animal positron emission tomography/magnetic resonance imaging (PET/MRI) detectors for operating in a high magnetic field, which use very small and thin scintillation pixels, is degraded at the periphery of the field of view (FOV). To solve this problem, we designed a detector that measures the depth of interaction (DOI) when gamma rays, a form of electromagnetic radiation, interact with scintillation pixels. The detector consists of four layers of quasi-block scintillators with photosensors with no signal distortion in a magnetic field at both ends of each layer, and the location of scintillation events was determined using a lookup table and maximum likelihood position estimation (MLPE). DETECT2000 simulation was performed to evaluate the performance of the designed detector. A lookup table was created using the light signals collected from the photosensors, and the location was determined by comparing it with new signals with reference to the MLPE. As a result, the discrimination accuracy was excellent at 92.0%. The application of this detector to small animal PET/MRI is expected to deliver outstanding spatial resolution.

Keywords: PET/MRI, high magnetic field, MLPE, DOI, DETECT2000

1. Introduction

In nuclear medicine systems designed to image small animals, image resolution is important. The organs and systems of small animals are very small compared to those in the human body, thus a system with excellent resolution is required to image them. Among these systems, positron emission tomography/magnetic resonance imaging (PET/MRI) for small animals also requires excellent resolution for imaging, which requires a highresolution PET detector operating in high magnetic fields. These detectors use scintillation pixels with very small cross-sections to improve the resolution. In fact, the smaller the scintillation pixels are, the higher the resolution of the acquired images. A PET image is acquired by using a radionuclide that emits positrons, and the image is obtained by detecting the annihilation radiation emitted from the source. This is high-energy electromagnetic radiation in the form of 511 keV gamma rays, thus a long scintillation pixel must be used to detect them in a PET detector. Therefore, to detect high-energy gamma rays and achieve high resolution, the scintillation pixels of a PET detector for small animals have small cross-sections and elongated shapes. PET systems equipped with scintillation pixels such as these have a high probability of detecting gamma rays emitted from the center of the field of view (FOV) by a single scintillation pixel, because these gamma rays are perpendicularly incident on the scintillation pixel. On the other hand, gamma rays emitted from the periphery of the FOV are obliquely incident on the scintillation pixel of the detector. In this case, they would be detected by adjacent scintillation pixels by penetrating scintillation pixels with a small cross section, that is, they have a high probability of being detected by multiple scintillation pixels. Detection by multiple scintillation pixels has the effect of lowering the spatial resolution when reconstructing the image, as shown in Fig. 1. Even when a detector with excellent resolution is used to image small animals, the resolution is reduced due to the high penetration power of highenergy gamma rays. Much research has been conducted in an attempt to solve this problem of the reduction of the

©The Korean Magnetics Society. All rights reserved.

*Corresponding author: Tel: +82-33-540-3384

e-mail: baekch@kangwon.ac.kr

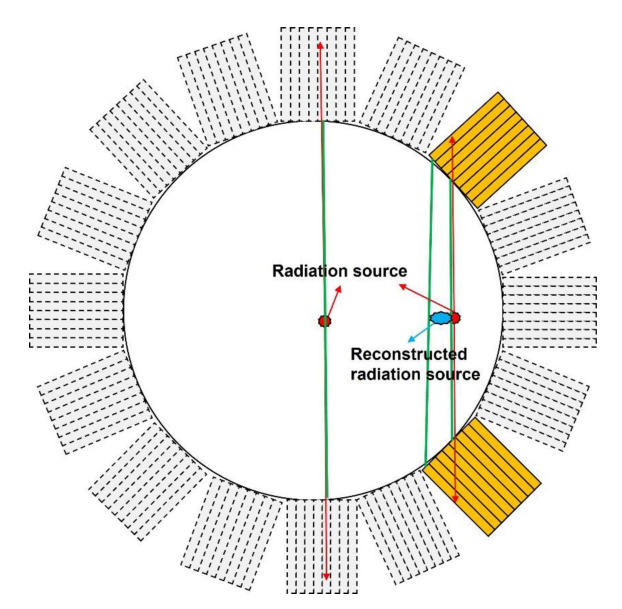


Fig. 1. (Color online) Decreased spatial resolution in the periphery of the FOV, where gamma rays from multiple scintillator pixels can be detected, which lowers the spatial resolution.

spatial resolution, and various detectors with improved spatial resolution have been developed. These detectors can be classified into three types. Detectors of the first type have scintillator blocks composed of scintillation pixels that are stacked in multiple layers and the gamma rays measured at each layer are classified [1-5]. The second type has a single layer of scintillator pixels with photosensors placed at both ends of the layer to measure the position where the gamma ray interacts with the scintillator pixels by determining the ratio of the signal intensity collected by the photosensors [6-9]. In the third type, the position where the gamma ray interacts with the scintillator pixels can be measured by arranging detectors consisting of scintillator blocks and photosensors in multiple layers [10, 11].

This study led us to propose a detector with improved performance based on the depth of interaction (DOI) detector we previously designed using a quasi-block scintillator [12]. In order to achieve high resolution, the area of the scintillation pixel where the gamma rays are incident must be small. Therefore, excellent spatial resolution can be achieved by using fine scintillation pixels. However, when using very small scintillation pixels, the ratio of the area occupied by the scintillation pixels to the detector area decreases. This is because the area of the reflector inserted between the scintillation pixels increases. As the area of the scintillator decreases, the sensitivity decreases, so a quasi-block scintillator was used to increase both the sensitivity and the spatial

resolution. The previous detector consisted of four layers of quasi-block scintillators, with a photosensor placed on each side to collect the light signal generated by the interaction with the gamma rays, identify the DOI layer, and obtain a flood image. Placing photosensors on each side requires a large number of photosensors, which can complicate the circuit configuration and increase the manufacturing costs. To address these shortcomings, in this study, the scintillator block is constructed by using four layers of quasi-block scintillators, the same as in the previous study, and signals are collected by only placing photosensors along both sides of the block. The signals collected from both ends are designed to visualize the location by applying the maximum likelihood position estimation (MLPE) [13, 14] and measure the DOI. The use of only two photosensors lowers the cost contribution of the photosensors, and accordingly, the circuit configuration is simplified and the overall cost of the detector is reduced. In previous studies, photosensors were used on all sides of the quasi-block scintillator, that is, four photosensors. In this design, signals generated by four photosensors must be collected. However, if two photosensors are used, only signals generated by two photosensors need to be collected, so the circuit for processing the signals of the photosensors becomes simpler. Additionally, a semiconductor photosensor was used to collect and process signals without distortion within a magnetic field. To evaluate the performance of the designed detector and confirm its usability, we used the simulation tool DETECT2000 [15, 16], which can simulate light in a scintillator-based detector.

2. Materials and Methods

2.1. Detector design

The detector that was designed to solve the spatial resolution degradation phenomenon in a PET system for small animals is shown in Fig. 2. The detector consists of four layers of quasi-block scintillators, and photosensors are positioned on both sides of the scintillator block to collect the light generated by the interaction between gamma rays and the scintillator. The quasi-block scintillator has a size of 12.6 mm × 12.6 mm × 3 mm and consists of a total of four layers, thus the size of the entire scintillator block is 12.6 mm \times 12.6 mm \times 12.6 mm. The gap between adjacent layers is designed to be 0.2 mm, which is the same as the gap between the photosensor pixels. The type of scintillator is a Gadolinium Aluminum Gallium Garnet (GAGG) scintillator with an ultrahigh density of 6.6 g/cm³ to detect high-energy gamma rays [17]. The GAGG scintillator has an excellent light output of 54,000

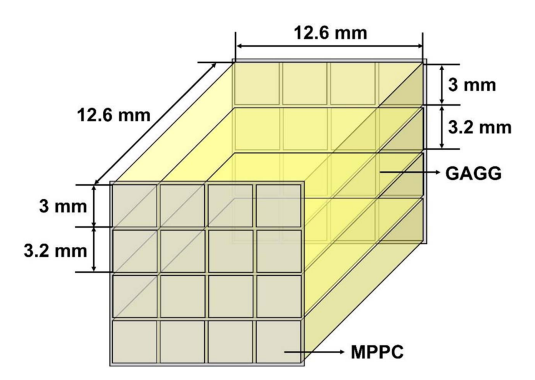


Fig. 2. (Color online) The detector we designed to solve the spatial resolution degradation of PET for small animals. The detector consists of a quasi-block scintillator with photosensors placed at both ends.

photons/MeV and, because it does not generate natural radiation, it can achieve excellent energy resolution. The semiconductor photosensor used was an MPPC with model number S14161-3050HS-04 from Hamamatsu [18]. This photosensor consists of a 4×4 array of pixels with an active area of 3 mm × 3 mm, and the gap between pixels is 0.2 mm to ensure that the overall size is the same as that of the scintillator block. The photosensor has a quantum efficiency of approximately 40% at 530 nm, which is the maximum wavelength of light generated from the GAGG scintillator. To transfer the light generated from the scintillator to the photosensor, all surfaces except the surface coupled to the photosensor were treated as reflectors, which were defined as diffuse reflectors. At the interface between the scintillator and photosensor, optical grease was applied to prevent the light collection efficiency from decreasing due to an abrupt change in the refractive index. The refractive index of the GAGG scintillator is 1.91, and that of the MPPC is 1.57. And an air layer is formed between the GAGG scintillator and the MPPC. The air layer has a refractive index of 1.0. Therefore, the light generated from the GAGG scintillator passes through the refractive index of 1.91, then the air layer with a refractive index of 1.0, and then enters the MPPC with a refractive index of 1.57. In other words, a rapid refractive index change occurs from 1.91 to 1.0, and a rapid refractive index change occurs from 1.0 to 1.57. This rapid change in refractive index causes total reflection of light, which reduces the collection efficiency of the MPPC.

2.2. DETECT2000 simulation and lookup table creation

The performance and usability of the designed detector was verified using the DETECT2000 simulator. The

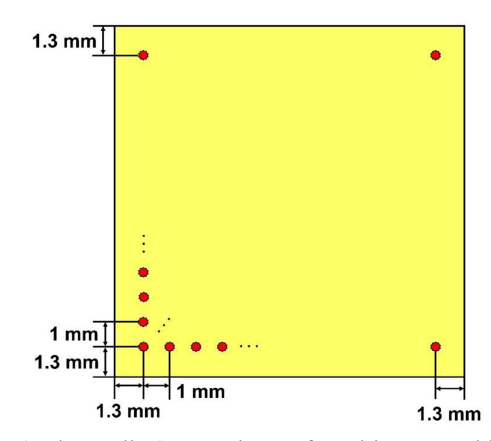


Fig. 3. (Color online) Locations of positions at which light was generated in simulations performed to verify and evaluate the performance of the designed detector.

DETECT2000 simulation tool can simulate the movement, scattering, absorption, and reflection of light within the scintillator of the detector, and enables materials to be configured by specifying their refractive index. The tool also allows the light measured by the scintillator to be simulated by configuring the photosensor. Using this simulator, the detector was designed, light was generated within the scintillator, light was collected by the light sensor to reconstruct the image, and the possibility of measuring the DOI was verified. The number of scintillation events generated within the scintillator took into account the light generation rate of the GAGG scintillator, the energy of the gamma rays, and the quantum efficiency of the photosensor. Fig. 3 shows the locations at which light was generated within the scintillator. Light was generated at 1 mm intervals from 1.3 mm to 11.3 mm from the edge of the scintillator, and the light was generated at the same location in each quasi-block scintillator. Light was repeatedly generated 1,000 times at each location. The light generated within the scintillator moves within the scintillator, is reflected by the reflector, and finally proceeds to the photosensor for detection. The light collected from the 32 pixels of each light sensor is reduced to four channels X+, X-, Z+, and Z- by assigning weights according to the location of the photosensor pixel, as shown in Fig. 4. This channel reduction was made in consideration of both the cost and the circuit: compared to using a collection circuit for all 32 channels, applying a collection circuit to 4 channels allows the circuit to be designed cost-effectively and with greater simplicity. In addition, the light signals collected from the photosensors located on both sides were collected as 2-channel signals. The signals collected through all 6 channels were calculated to calculate the mean and standard deviation of

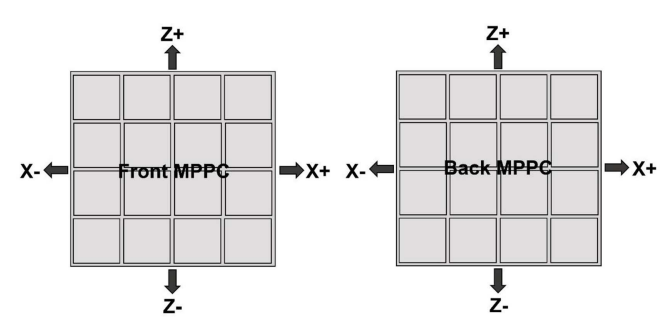


Fig. 4. Channel reduction through weighting according to the location of the photosensor pixels. A total of 32 channels corresponding to the two photosensors were reduced to 4 channels.

the signals, and this was performed for each location. Finally, the mean and standard deviation for each location were used to construct a lookup table and used for the MLPE.

2.3. Evaluation of locations of gamma-ray interaction by applying MLPE

The MLPE can be used to find the closest location by comparing previously stored data with newly input data. Using this, the location at which the gamma ray interacted can be determined by comparing the data input at the new location with all the previously created gamma ray event locations in the lookup table. The MLPE can be expressed as follows.

$$\ln \Pr\left[\frac{M_i}{x}\right] = -\left(\sum_{i=1}^n \frac{\left(M_i - \mu(x)\right)^2}{2\sigma_i^2(x)} + \sum_{i=1}^n \ln \sigma_i(x)\right) \tag{1}$$

Here, M represents the input data, and μ and σ

represent the mean and standard deviation written in the lookup table. The input data are compared with all data in the lookup table, and the value with the smallest difference among them is derived, and the location corresponding to the derived value at this time becomes the location at which the gamma ray interacted with the scintillator. Using the MLPE, the location can be distinguished even by a small difference. In other words, even in the case of a small difference in the overlapping location in the flood image, the overlap can be separated and the location can be derived.

3. Results

3.1. Creating the lookup table

A lookup table was constructed based on the light signals collected from the photosensors located at both ends of the scintillator block. The lookup table was built for a total of 6 channels, and was created with the 4channel signals for X+, X-, Z+, and Z- and the total signal collected from each photosensor. For each location within the scintillator where light was generated, signals for 6 channels were collected, and a lookup table was created with the mean and standard deviation for 1000 gamma events. Light was generated starting from 1.3 mm from the edge of the scintillator to 11.3 mm in 1 mm intervals; thus, entries for the lookup table were created for 11 × 11 locations for each quasi-block scintillator to ultimately construct a lookup table with entries for a total of 11 × 11 × 4 locations. Fig. 5 shows a part of the created lookup table to confirm that it contains the mean and standard deviation for each of the 6 channels.

Position (x, y, z)	1ch μ	1ch σ	2ch μ	2ch σ	3ch μ	3ch σ	4ch μ	4ch σ	5ch μ	5ch σ	6ch μ	6ch σ
(1, 1, 1)	33689.38	354.6739	58008.76	426.197	5088.475	47.52519	2189.155	41.76057	11603.4	77.7665	80097.36	413.581
(2, 1, 1)	35123.87	342.1931	56695.51	416.3883	5080.651	48.39799	2206.602	39.52776	11626.94	77.15571	80195.22	418.3944
(3, 1, 1)	37687.52	340.1805	53607.45	393.7613	5029.377	47.38823	2216.255	41.80363	11562.48	74.72324	79734.86	404.3902
(4, 1, 1)	40722.74	339.2784	51566.16	391.0435	5089.082	48.33497	2235.434	42.36473	11679.47	76.72303	80611.33	416.3868
(5, 1, 1)	43039.2	334.4126	49165.34	366.256	5073.14	45.87899	2244.681	41.20037	11669.29	73.12568	80535.85	395.2779
(6, 1, 1)	45648.22	350.5975	45650.51	356.0293	5010.704	48.04853	2235.227	41.58744	11564.57	76.42794	79734.81	407.0054
(7, 1, 1)	49187.92	360.8845	43044.6	353.7777	5074.47	47.76759	2245.571	42.14588	11672.98	75.65291	80558.92	413.0435
(8, 1, 1)	51584.41	372.408	40730.33	348.291	5089.734	45.58334	2236.833	40.43954	11682.21	78.92657	80630.64	400.147
(9, 1, 1)	53611.38	394.8301	37673.41	344.1687	5029.214	45.61316	2215.611	40.39212	11559.47	77.58607	79724.07	420.563
(10, 1, 1)	56719.9	397.9818	35121.55	343.9459	5083.824	46.52414	2205.18	40.55653	11624.98	71.98061	80214.31	401.4622
(11, 1, 1)	58029.66	437.0462	33688.26	349.609	5091.628	46.25124	2187.572	40.3693	11604.2	77.56158	80111.35	416.8373
(1, 2, 1)	35937.87	362.1886	55406.08	402.831	4775.819	45.35309	2473.701	40.66582	11515.37	74.71029	79829.83	403.7833
(2, 2, 1)	36527.33	340.5166	54330.04	407.1985	4776.864	46.12122	2434.038	41.67802	11469.71	76.80378	79388.93	414.1558
(3, 2, 1)	38364.49	353.554	52759.04	400.5373	4793.175	47.63046	2438.851	40.62279	11501.17	75.07928	79622.78	413.2675
(4, 2, 1)	40806.51	357.5492	50756.31	388.259	4809.127	47.23872	2457.764	41.91347	11568.05	76.16324	79995.94	412.1566
(5, 2, 1)	43236.78	354.4199	48295.48	364.9374	4802.635	48.54778	2461.83	42.81893	11564.87	76.45513	79967.92	410.986
(6, 2, 1)	45677.04	364.1964	45661.05	360.2783	4790.388	45.76569	2458.667	41.39483	11533.14	75.27548	79804.89	421.6772

Fig. 5. Part of a lookup table created from signals generated at each light source location and collected from the light sensors. The lookup table lists the mean and standard deviation that were calculated for each channel.

3.2. Evaluation of the locations of gamma-ray interaction

Based on the light signals generated by the simulator at each location in the scintillator, the lookup table was created, and the location of each light signal was determined using the MLPE for this lookup table and the simulation data. Fig. 6 shows a flood image reconstructed using data acquired at all locations in all layers where light was generated. (a) is an image for the XY plane, (b) is an image for the YZ plane, and (c) is an image for the XZ plane. In the XY plane, it can be confirmed that the gamma-ray event locations overlap in the edge area of the scintillator in the X-axis direction. In particular, the image confirms that the overlap becomes more severe toward the center of the flood image. Fig. 7 shows the profile along the Y-axis of the centerline in the flood image in Fig. 6(a), and confirms that the locations of the two edges completely overlap. Additionally, the image in the YZ plane is completely separated into the Y- and Z-axes and, because the quasi-block scintillator is completely separated from the reflector in the Z-axis, the results confirm that it is also completely separated in the flood image. The image in the XZ plane is confirmed to be completely separated along the Z-axis as in the YZ plane, but it overlaps along the X-axis. This result is a consequence of the image being reconstructed in a barrel shape in the XY plane. With this approach, it can be confirmed that the overlap in the edge part of the scintillator is clearly shown in the generally reconstructed flood image. Table 1 presents the accuracy of each position for all layers determined by the MLPE and confirms that the accuracy in the edge area is relatively low. This is related to the result of the overlap in the edge area in the flood image. The overlap in the image is due to the high similarity of the acquired signals. Therefore, the accuracy was measured to be relatively low in the position determination

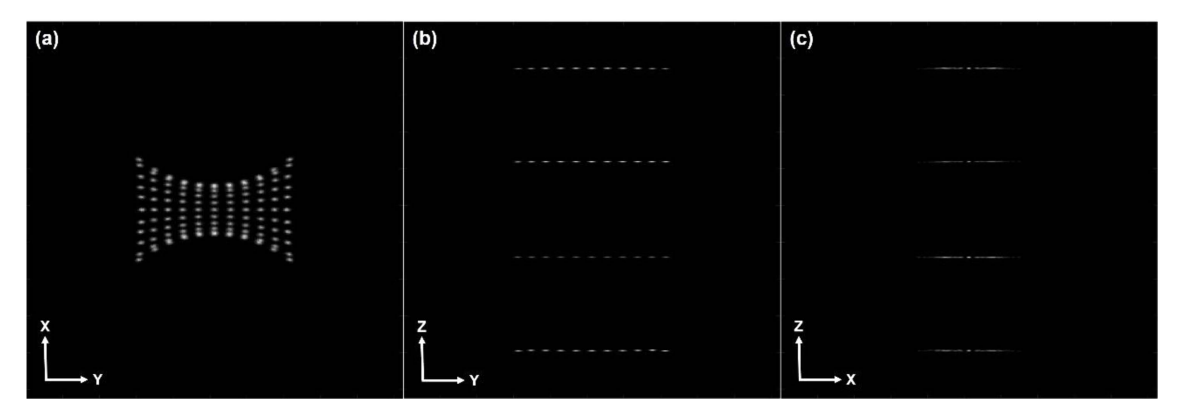


Fig. 6. Flood images reconstructed by collecting light generated from the quasi-block scintillator. Flood images in the (a) XY-, (b) YZ-, and (c) XZ-planes.

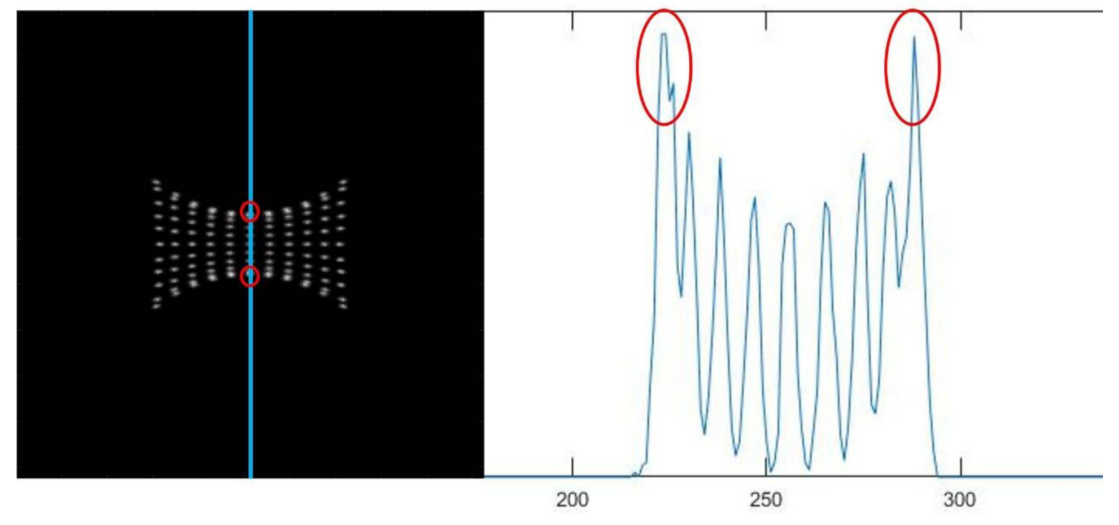


Fig. 7. (Color online) Profile along the Y-axis of the centerline in the plane image of Fig. 6(a) showing that two edge points overlapped.

Table 1.	Accuracy	for	all	lavers	in	the	XY	plane.

					Accura	acy (%)					
	X1	X2	X3	X4	X5	X6	X7	X8	X9	X10	X11
Y1	98.9	98.9	98.2	98.0	98.4	97.9	98.6	98.4	98.5	99.1	99.2
Y2	92.6	92.3	96.7	96.9	96.0	95.0	96.8	97.1	97.1	93.0	93.5
Y3	83.8	80.8	97.4	96.8	95.4	95.2	96.1	97.1	97.1	81.2	83.6
Y4	78.5	74.6	93.7	96.6	95.9	97.2	97.7	93.7	93.7	75.9	79.6
Y5	76.5	70.6	91.5	97.4	98.5	98.4	98.9	93.1	93.1	72.1	77.0
Y6	76.4	70.4	90.5	97.7	98.8	99.2	99.2	90.6	90.6	71.9	76.3
Y7	78.2	71.6	91.2	98.2	99.3	97.7	99.0	92.2	92.2	71.0	76.9
Y8	78.6	75.0	93.3	98.1	97.5	97.0	97.4	94.3	94.3	73.7	78.1
Y9	83.6	80.7	97.2	97.1	96.2	95.4	96.2	96.4	96.4	79.4	82.2
Y10	90.3	92.4	96.5	96.9	96.1	95.7	96.0	96.8	96.8	92.1	92.5
Y11	99.0	98.7	97.4	98.0	98.3	97.6	98.6	98.1	98.1	98.7	98.9

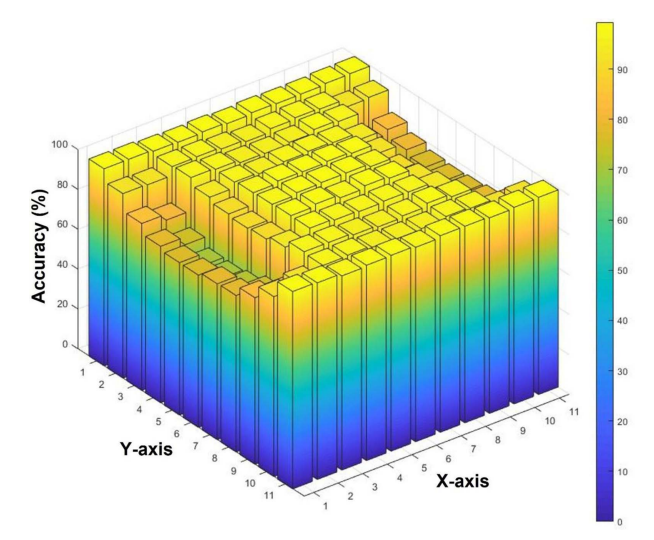


Fig. 8. (Color online) Positional accuracy determined by MLPE for positions in the XY-plane. Overlapping regions at the edges are responsible for degrading the accuracy in these regions.

using the MLPE. However, although the flood image appeared as a completely overlapped image, the position determination ability of the MLPE was relatively excellent with a minimum accuracy of 70.4%. Fig. 8 shows the accuracy of all layers for the position determination in the XY plane, from which it is evident that the edge part is measured with relatively low accuracy compared to the center. Fig. 9(a) shows the accuracy along the Y-axis line in Fig. 8, which shows that the accuracy is relatively low in the center and excellent at the edges. This is considered to reflect the fact that the degree of overlap in the flood image becomes more prominent toward the center. Fig. 9 (b) shows the accuracy along the X-axis line. Mirroring the overlap of the edges in the flood image, the accuracy of the position determination through the MLPE is relatively low at the two points along the edge and excellent in the center. Fig. 10 shows the position determination obtained by calculating the MLPE for the

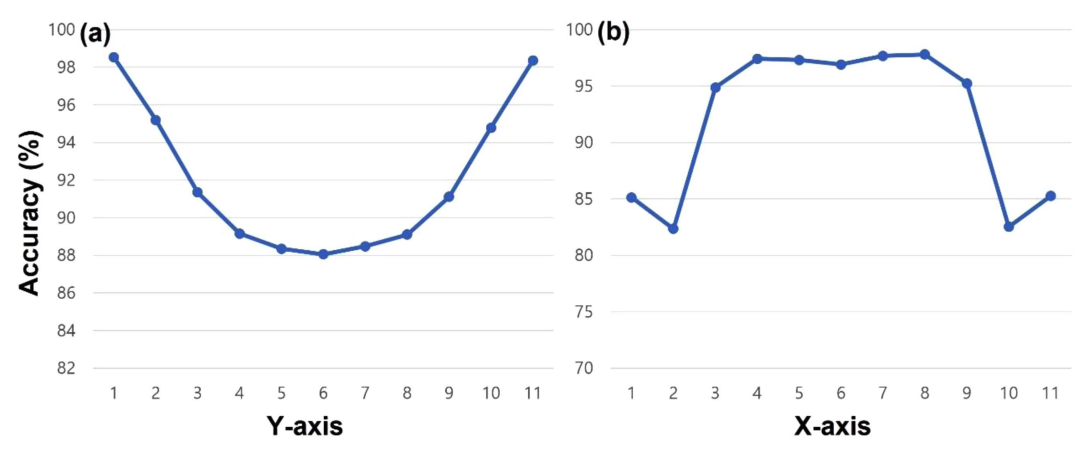


Fig. 9. (Color online) Integrated accuracy plot for each location along the X- and Y-axes in Fig. 8. Accuracy corresponding to the (a) Y-axis and (b) X-axis.

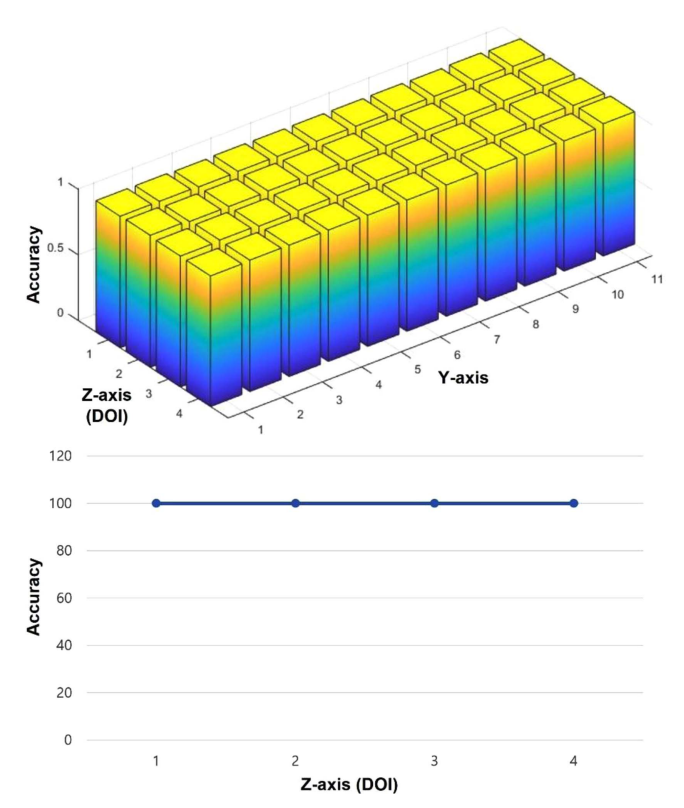


Fig. 10. (Color online) Accuracy of DOI measurement as determined by MLPE, confirming that the layer discrimination is perfect.

XZ plane, and shows that the DOI layers, which are stacked along the Z-axis, are perfectly distinguishable.

4. Discussion and Conclusions

We designed a small animal PET detector that performs position discrimination by arranging photosensors at both ends of a quasi-block scintillator and using MLPE. For the XZ-axis, a lookup table was created using the signals acquired from the photosensors at both ends. These signals were summed and reduced into four channels, and a lookup table for the Y-axis was created by summing these signals. The locations of the light signals detected at all positions were discriminated with the aid of the created lookup table and the MLPE. The overall position discrimination accuracy of 92.0% confirms the excellent position discrimination ability of the detector. The overlapping flood images generated near the periphery of the scintillator mean that the light signals collected from this area could not be clearly distinguished. This was also evident from the position discrimination accuracy of MLPE, which could not clearly distinguish two points located near the edge, with relatively low position discrimination accuracy. In the flood image, they were completely overlapped, which means that they could not be distinguished at all; however, with MLPE, a minimum of 65.6% compliance was obtained at the second location of the sixth line of the Y-axis on the third DOI level. Relatively excellent location discrimination is considered to be achievable by determining the location using MLPE, even in a perfectly overlapped location. The simulation was performed at 1 mm intervals. The images for the corresponding locations are shown in Fig. 6(a). There is some overlap at the edge of the center. However, all other locations are separated. Therefore, it is expected that a spatial resolution of at least 1 mm can be secured. The application of this detector design to a PET system for small animals is expected to enable a more compact detector to be developed. This is because the cost can be reduced by limiting the use of photosensors and by ensuring the simplicity of the signal processing circuit. In addition, because the DOI can be measured, the phenomenon of reduced spatial resolution that occurs along the periphery of the FOV is expected to be resolved.

Acknowledgments

This work was conducted during the sabbatical year of Dongseo University in 2025.

References

- [1] H. Liu, T. Omura, M. Watanabe, and T. Yamashita, Nucl. Instrum. Methods Phys. Res. A **459**, 182 (2001).
- [2] M. Ito, J. S. Lee, S. I. Kwon, G. S. Lee, B. Hong, K. S. Lee, K-S. Sim, S. J. Lee, J. T. Rhee, and S. J. Hong, IEEE Trans. Nucl. Sci. 57, 976 (2010).
- [3] H. Murayama, I. Ishibashi, H. Uchida, T. Omura, and T. Yamashita, IEEE Trans. Nucl. Sci. 45, 1152 (1998).
- [4] T. Tsuda, H. Murayama, K. Kitamura, T. Yamaya, E. Yoshida, T. Omura, H. Kawai, N. Inadama, and N. Orita, IEEE Trans. Nucl. Sci. 51, 2537 (2004).
- [5] B. Jo and S-J. Lee, Nucl. Eng. Technol. 57, 103409 (2025).
- [6] Y. Shao, R. W. Silverman, R. Farrell, L. Cirignano, R. Grazioso, K. S. Shah, G. Vissel, M. Clajus, T. O. Tumer, and S. R. Cherry, IEEE Trans. Nucl. Sci. 47, 1051 (2000).
- [7] Y. Shao, H. Li, and K. Gao, Nucl. Instrum. Methods Phys. Res. A 580, 944 (2007).
- [8] J. Du, IEEE Trans. Radiat. Plasma Med. Sci. **6**, 522 (2021).
- [9] R. Cheng, M. Sun, F. Wang, D. Mu, Y. Liu, Q. Xie, B. Qiu, X. Chen, and P. Xiao, IEEE Trans. Radiat. Plasma Med. Sci. 8, 709 (2024).
- [10] C. S. Levin, IEEE Trans. Nucl. Sci. 49, 2236 (2002).
- [11] A. Vandenbroucke, A. M. K. Foudray, P. D. Olcott, and

- C. S. Levin, Phys. Med. Biol. 55, 5895 (2010).
- [12] S-J. Lee and B. Jo, J. Korean Soc. Radiol. 18, 65 (2024).
- [13] H. H. Barrett, W. C. J. Hunter, B. W. Miller, S. K. Moore, Y. Chen, and L. R. Furenlid, IEEE Trans. Nucl. Sci. **56**, 725 (2009).
- [14] Y. H. Chung, S.-J. Lee, C.-H. Baek, and Y. Choi, Nucl. Instrum. Methods Phys. Res. A 593, 588 (2008).
- [15] F. Cayouette, D. Laurendeau, and C. Moisan, Proc. SPIE, Quebec 4833, 69 (2003).
- [16] F. Cayouette, C. Moisan, N. Zhang, and C. J. Thompson, IEEE Trans. Nucl. Sci. 49, 624 (2002).
- [17] J. Y. Yeom, S. Yamamoto, S. E. Derenzo, V. C. Spanou-daki, K. Kamada, T. Endo, and C. S. Levin, IEEE Trans. Nucl. Sci. 60, 988 (2013).
- [18] https://www.hamamatsu.com/content/dam/hamamatsu-photonics/sites/documents/99_SALES_LIBRARY/ssd/s14160 s14161 series kapd1064e.pdf